Robust segment-type energy harvester and its application to a wireless sensor

2009 Smart Mater. Struct. 18 095021

(http://iopscience.iop.org/0964-1726/18/9/095021)

Smart Mater. Struct. **18** (2009) 095021 (12pp) doi:10.1088/0964-1726/18/9/095021

Robust segment-type energy harvester and its application to a wireless sensor

Soobum Lee, Byeng D Youn[1] and Byung C Jung

Department of Mechanical Engineering, University of Maryland, College Park, MD 20742, USA

E-mail: bdyoun@umd.edu

Received 17 January 2009, in final form 17 June 2009
Published 17 July 2009
Online at stacks.iop.org/SMS/18/095021

Abstract

This paper presents an innovative design platform of a piezoelectric energy harvester (EH), called a segment-type EH, and its application to a wireless sensor. Energy harvesting technology is motivated to minimize battery replacement cost for wireless sensors, which aims at developing self-powered sensors by utilizing ambient energy sources. Vibration energy is one of the widely available ambient energy sources which can be converted into electrical energy using piezoelectric material. The current state-of-the-art in piezoelectric EH technology mainly utilizes a single natural frequency, which is less effective when utilizing a random ambient vibration with multi-modal frequencies. This research thus proposes a segment-type harvester to generate electric power efficiently which utilizes multiple modes by separating the piezoelectric material. In order to reflect the random nature of ambient vibration energy, a stochastic design optimization is solved to determine the optimal configuration in terms of energy efficiency and durability. A prototype is manufactured and mounted on a heating, ventilation, air conditioning (HVAC) system to operate a temperature wireless sensor. It shows its excellent performance to generate sufficient power for real-time temperature monitoring for building automation.

(Some figures in this article are in colour only in the electronic version)

1. Introduction

The continual advances in wireless technology and low power electronics have allowed the deployment of small remote sensor networks for various applications including environmental monitoring, gas and chemical sensors, motion detectors, structural health monitoring and explosives detection. Current wireless devices must be designed to include electrochemical batteries as the power source. But the use of batteries can be troublesome due to their limited lifespan, especially when their replacement in inaccessible and remote locations is required. Furthermore, the battery replacement costs $80–$500 including labor and it exceeds the price of a sensor [1]. This issue has spawned the rapid growth of the energy harvesting field. Energy harvesting devices are designed to capture the ambient energy surrounding the electronics and convert it into usable electrical energy. The concept of energy harvesting works towards developing self-powered devices that do not require replaceable power supplies. A number of harvestable ambient energy sources exist, including waste heat, vibration, electromagnetic waves, wind, flowing water and solar energy. While each of these sources of energy can be effectively used to power remote sensors, vibration energy has gained much attention due to its widespread availability.

Mechanical vibrational energy can be converted to electrical energy using electrostatic, electromagnetic or piezoelectric energy conversion. Among these, piezoelectricity is the ability of some materials to generate an electric potential in response to applied mechanical stress, and its energy conversion can be said to combine most of the advantages of both electromagnetic and electrostatic converters [2]. It has been studied to compare piezoelectric, electromagnetic and electrostatic configurations as a means of harvesting energy from a variety of vibration sources. This study showed that piezoelectric materials are the simplest and most practical way of conversion [3–5]. Piezoelectric materials includes PZT (lead zirconate titanate), ZnO (zinc oxide) and PVDF (polyvinylidene difluoride), and PZT is known to possess the best conversion efficiency among them [5].

[1] Author to whom any correspondence should be addressed.

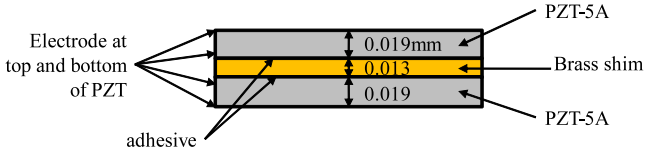

Figure 1. Cross section of piezoelectric bimorph.

Table 1. Specification of piezoelectric bimorph.

Dimension	Size (mm)
Length	63.5
Width	31.8
PZT thickness	0.019
Brass thickness	0.013

1.1. Literature survey

A typical energy harvester (EH) using piezoelectricity is a cantilever unimorph/bimorh and it generates AC voltage proportional to the bending strain of the piezoelectric material. Glynne-Jones *et al* [3] screen-printed PZT on a 23 × 23 mm^2 stainless steel cantilever plate to get a power of 3 μW under resonant vibration. Leland *et al* manufactured a piezoelectric EH using PZT-5A4E, brass and a mass made of tungsten [6]. They generated a power of 29.3 μW using vibration from human walking for 50 min. Roundy *et al* manufactured a cantilever-type EH using PZT and PVDF and performed design optimization to obtain high power output with the change of mass, cantilever length, piezoelectric material thickness and external resistance value [7]. Sodano *et al* formulated a model of an energy harvesting system that consists of a cantilever beam with piezoelectric patches attached and experimentally verified it [8]. Chen *et al* proposed the relationship between the deduced voltage and the mechanical strain in a cantilever bimorph microtransducer [9]. Elvin *et al* [10] developed a self-powered damage detection unit for energy generation and storage using PVDF. The performance of the sensor was illustrated in terms of sensing and wirelessly communicating data about the damage state of a structure to a remote receiving unit.

The studies on the optimal shape of a cantilever EH have been done where a rectangular and a trapezoidal shape of piezoelectric beam shape were mostly compared in terms of tolerable amplitude and output power under vibration. Most works on this problem showed that a trapezoidal shape was more efficient because of a uniformly large strain at every point on the beam surface [3, 11, 12]. Zheng *et al* suggested a topological optimum design to maximize energy conversion [13], but this design raised additional manufacturing issues. The amount of power generated by piezoelectric EHs has been evaluated in a number of studies. Umeda *et al* conducted a study into the characteristics of energy storage by a piezo-generator with a bridge rectifier and capacitor [14]. The piezo-generator consisted of a steel ball and a piezoelectric vibrator, a bridge rectifier and capacitor. To simulate the generation and storage mechanism they employed an equivalent circuit model and showed that their prototype achieved a maximum efficiency of 35%. Sodano *et al* studied the storage of electrical energy from energy harvesting devices in batteries and capacitors [15], and characterized several commercial piezoelectric materials for energy harvesting applications [16, 17]. Using the EHs developed above, some ambient vibration sources have been found and utilized for electric energy generation mainly from machinery and human movement (several vibration sources are well introduced in the references [2, 12]). Granstrom *et al* developed a piezoelectric polymer backpack strap which generated electrical energy from the oscillating tension in the strap during walking [18]. Leland *et al* mounted an EH on a wooden staircase and generated electricity from vibrations in the staircase to get around 30 μW [6]. Some case studies of energy harvesting from vehicle engine vibration and bridge vibration is found on a website [19]. Shoe-mounted EH is another example of EH which utilized human movement; pressure by heel strikes [20, 21]. Recent studies on piezoelectric EHs are well summarized in review articles [12, 22, 23].

1.2. Motivation and objective

Most of the previous works have mainly focused on a simple cantilever-type harvester [3, 6–9, 11] and many theoretical models have been developed mainly based on a simple geometry such as a uniform cantilever beam. However this design is tailored to operate only at a single resonant frequency, so it uses a small fraction of ambient vibration energy since the ambient vibration has multiple resonant peaks. This paper aims at developing a new design platform of EH, which makes use of multiple resonant frequencies. This EH design platform allows additional scavenging of ambient energy from a higher resonant frequency. A simulation model for a new conceptual design of EH is constructed and a detailed design task is performed by design optimization technique. In detail, a valid FE model for the piezoelectric coupled analysis was constructed for accurate prediction of the performances of any EH design, and design optimization was performed to maximize the electrical power while considering the randomness of ambient vibration, structural durability and manufacturability. The optimization result was manufactured and attached on the HVAC (heating, ventilation, air conditioning) system in a building for operating a wireless sensor as a case study.

This paper is organized as follows: the construction of a reliable simulation model (section 2), proposition of a segment-type design platform and its design optimization (section 3), prototype manufacture (section 4) and its performance evaluation (section 5), and a real-world application to operate a temperature wireless sensor (section 6).

2. Construction of parametric computer model

2.1. FE model for piezoelectric coupled analysis

A reliable computer model is required for exploring many EH designs. In this section, a piezoelectric bimorph specimen from Piezo System Inc. [24] (see table 1 and figure 1) is used as a basis of FE modeling for piezoelectric coupled analysis. The specimen is composed of 9 layers in total as shown in figure 1:

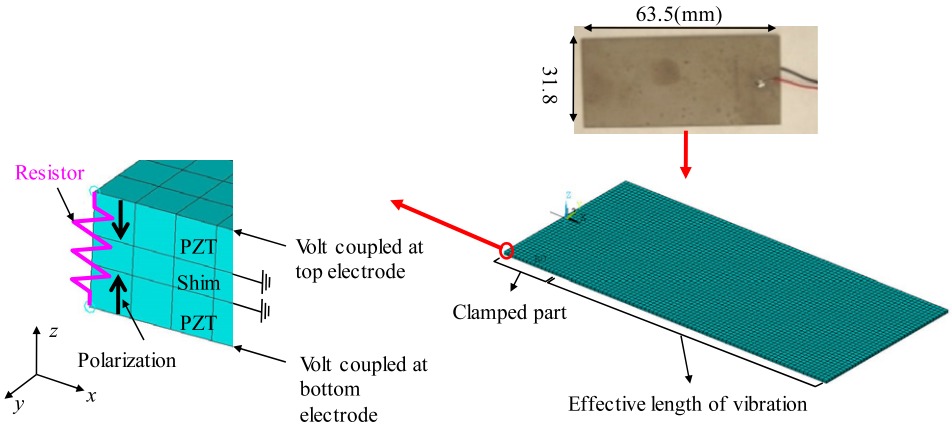

Figure 2. FE modeling of series operated bimorph.

two PZT plates (with PZT-5A and two nickel electrode layers), a center brass shim and two conductive adhesive layers. The nickel electrodes and adhesive are ignored in the FE model because of their ignorable thickness in the simulation, and perfect bonding condition is assumed. The FE model was developed using ANSYS, as shown in figure 2. The PZT plates were modeled using a SOLID5 element with four coupled-field degrees of freedom (DOFs) (three translational DOFs and one electrical potential DOF), and the center shim by a SOLID45 element with three translation DOFs. The specimen harvests energy using the '31' mode when it extends or compresses in the x direction (due to a bending in the y direction) and, as a result, voltage drop is generated in the z direction (see figure 2 for axes). The specimen with series operation is modeled by two facing polarization axes (along the z direction). The series operation is chosen because the sensor node selected for a case study in section 6 requires relatively high voltage; the series operation generates a voltage twice as high as the parallel operation. The two electrode surfaces facing the center shim are grounded. The voltage degrees of freedom at the finite element nodes on both top and bottom surfaces are coupled to simulate the electrodes. These two electrodes are connected with a resistance, which is the input impedance of the measurement equipment (data acquisition board: NI PCI-6251 [25]).

2.2. FE Model calibration

In this section the FE model for a PZT bimorph cantilever is calibrated—the difference between the experimentally measured performances and the predicted performance in the simulation is minimized by adjusting the PZT material properties. A mechanical damping ratio is measured by applying an impulse and calculated as a function of the log decrement of the two magnitudes as shown in (1) [26]:

$$\zeta = \frac{1}{2\pi N} \log \frac{x_0}{x_N} \tag{1}$$

where x_0 and x_N are the vibration magnitude at a point and after a period N later. In this study ζ is repeatedly measured (50 times) and the average value (=1.98%) is used. The electric wires are soldered on the top and bottom electrode surfaces, as shown in figure 2.

The model calibration is decomposed into two steps [27]: the first step for mechanical performance (resonant frequencies) and the second step for electrical performance (open circuit voltage spectrum). The resonant frequency is tuned under a mass constraint (or mass manufacturing tolerance) in the first step so that the Young's modulus and the density are adjusted, while the voltage spectrum in a frequency domain is adjusted to match the test results in the second step. For each step the calibration is formulated as an optimization problem as described in (2), where p_i is the calibration parameter, $F(p_i)$ is the performance with the target F_t and p_i^0 is the initial value of p_i:

$$\begin{aligned} &\min\{F(p_i) - F_t\}^2 \\ &s.t. \quad 0.9p_i^0 \leqslant p_i \leqslant 1.1p_i^0. \end{aligned} \tag{2}$$

The lower and upper bound of p_i is set as 90% and 110% of p_i^0. The initial values are taken from [28, 29] where the parameters include the strain compliance matrix (s^E), permittivity matrix (ε^T) and piezoelectric matrix (d). They are shown in the constitutive equations of linear piezoelectricity written as follows:

$$\begin{aligned} S &= s^E\sigma + \mathrm{d}E \\ D &= \mathrm{d}\sigma + \varepsilon^T E \end{aligned}$$

$$s^E = \begin{bmatrix} s_{11} & s_{12} & s_{13} & 0 & 0 & 0 \\ & s_{11} & s_{13} & 0 & 0 & 0 \\ & & s_{33} & 0 & 0 & 0 \\ & & & s_{44} & 0 & 0 \\ & sym & & & s_{44} & 0 \\ & & & & & s_{66} \end{bmatrix},$$

$$d = \begin{bmatrix} 0 & 0 & d_{31} \\ 0 & 0 & d_{31} \\ 0 & 0 & d_{33} \\ 0 & d_{15} & 0 \\ d_{15} & 0 & 0 \\ 0 & 0 & 0 \end{bmatrix}, \tag{3}$$

$$\varepsilon^T = \begin{bmatrix} \varepsilon_{11} & 0 & 0 \\ & \varepsilon_{11} & 0 \\ sym & & \varepsilon_{33} \end{bmatrix}$$

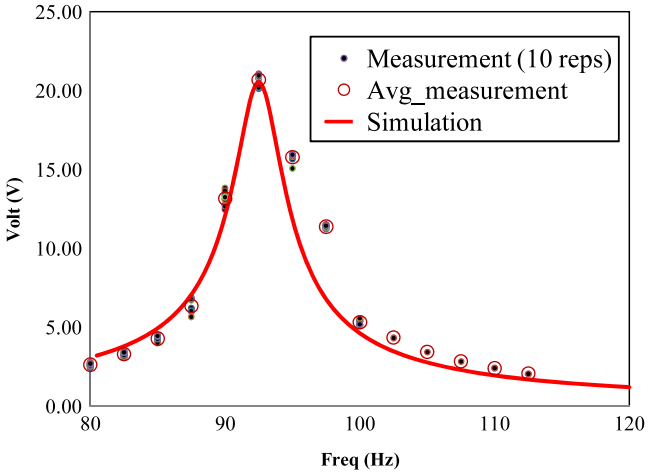

Figure 3. Modal calibration to match open circuit voltage.

where S and σ are the mechanical strain and stress tensors, and E and D are the electric field and displacement tensors, respectively.

In the first step, the modal tests were done 50 times to measure the target frequency and its average value (F_t) is 92.8 Hz with its measurement error of 1.77 Hz. The mass is limited to be in the bounds of 8.0 ± 0.1 g (8.0 g is provided in the specimen catalog and ± 0.1 g is manufacturing tolerance). The parameters of density and modulus of elasticity are chosen as calibration parameters. Brass is an isotropic material and we have two calibration parameters in this material (density and modulus of elasticity: ρ_b and Y_b). On the other hand, a PZT layer is anisotropic as shown in s^E from (3) and we have six parameters for the calibration: ρ_p (density), s_{11}, s_{12}, s_{13}, s_{33}, s_{44} and s_{66}. The parameters in the piezoelectric matrix ($d_{31}, \underline{d}_{15}$) have very low sensitivity on the natural frequency based on the numerical sensitivity analysis using the FE model, so they are not considered as calibration parameters in this step.

For the measurement of the target voltage in the second step, the shaker is excited at the resonant frequency (92.8 Hz) under $1g$ acceleration (a unit acceleration of gravity) so that the specimen produces AC voltage. The AC voltage is measured between top and bottom surfaces of the specimen. In the simulation, harmonic response analysis is done and the steady state response of voltage amplitude is obtained. The

Table 2. Parameter adjustment by model calibration.

Step	Parameter	Value after calibration
First—resonant frequency	ρ_b	9133 kg m^{-3}
	ρ_p	7171 kg m^{-3}
	Y_b	126.5 GPa
	s_{11}	1.7605×10^{-11} m^2 N^{-1}
	s_{12}	-5.166×10^{-12} m^2 N^{-1}
	s_{13}	-7.942×10^{-12} m^2 N^{-1}
	s_{33}	1.692×10^{-11} m^2 N^{-1}
	s_{44}	4.275×10^{-11} m^2 N^{-1}
	s_{66}	4.873×10^{-11} m^2 N^{-1}
Second—voltage	d_{31}	-1.539×10^{-10} m V^{-1}
	d_{33}	4.114×10^{-10} m V^{-1}
	ε_{33}	916.0

components in the piezoelectric matrix (d) and the permittivity matrix (ε^T in (3)) are chosen as the parameters for calibration in this step, a total of five parameters. Among them, based on sensitivity analysis, d_{31}, d_{33} and ε_{33} are chosen as the calibration parameters. The calibration result is shown again in table 2. Figure 3 shows the voltage spectrum around the resonant frequency as a result of the calibration. The solid line is the voltage spectrum from the calibrated FE model while the dots indicate each experimental measurement. The simulation results show an excellent agreement with the measured data. This calibration results are used in the FE model in section 3.

3. Stochastic design optimization of segment-type EH

3.1. Segment-type EH platform to eliminate cancelation

Most piezoelectric EHs developed to date are a cantilever type, which is tailored to operate best at a single resonant frequency (e.g. the first natural frequency of the cantilever). The electric voltage generation from a bimorph is explained in figure 4. A bimorph is composed of two PZT plates attached on the top and bottom surface of the center shim (brass or stainless steel). In the first mode of vibration (figure 4(a)), top and bottom PZT plates experience compressive (indicated by plus sign) and tensile (minus sign) strain, respectively. The other opposite configuration, tension on the top and compression on the bottom PZT segment, occurs and these two configurations are repeatedly alternating. Because there

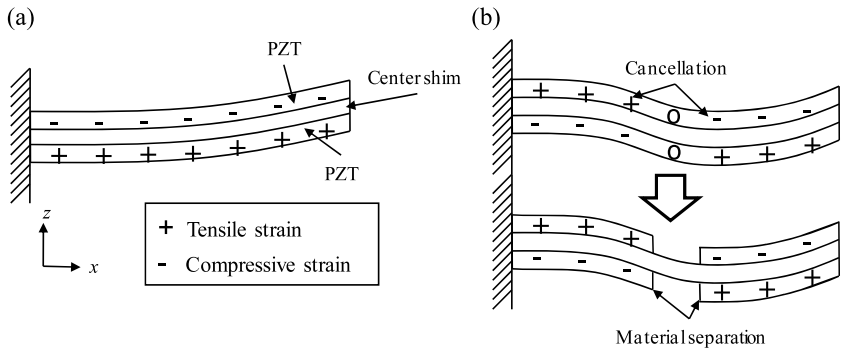

Figure 4. Cancelation effect. (a) First mode, (b) second mode.

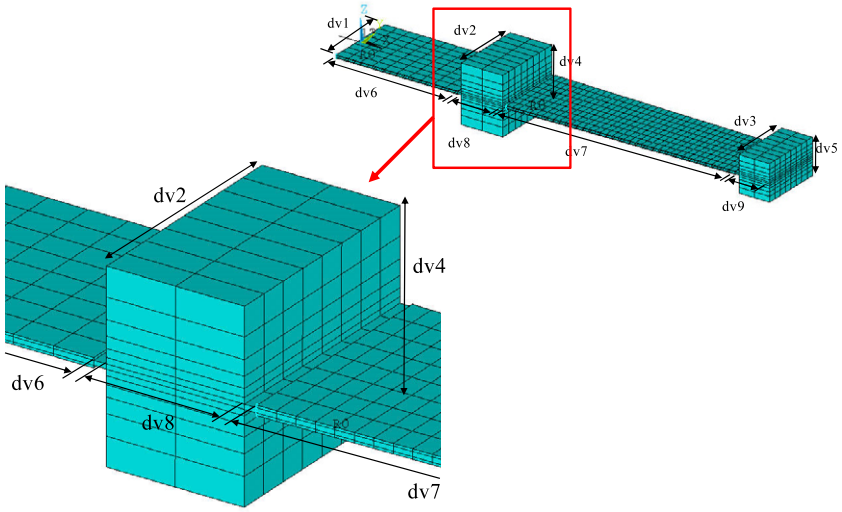

Figure 5. Design variables indicated in the initial model.

is no sign change of strain on each PZT plate, the electric energy is generated proportional to the strain without electrical charge cancelation. In the second mode, however, an inflection point occurs in the middle of the cantilever where the curvature sign of deformation changes, and it eliminates the electricity generation because of charge cancelation as shown in the upper part of figure 4(b). The charge cancelation is a disadvantageous feature of a cantilever EH because it cannot capture the higher-mode vibration energy from a real-world excitation condition. That is why this paper proposes a new design platform of EH for utilizing an ambient vibration energy at multi-modal harmonic frequencies.

In the second mode as shown in figure 4(b), tension and compression may occur simultaneously in one PZT plate, thus causing partial cancelation of the electrical charge (or energy). It means we cannot maximally exploit the second or higher vibration mode of the cantilever for energy harvesting. To prevent this, a PZT plate is separated at an inflection point so that each PZT segment experiences either tensional or compressive strain at an instantaneous time. Two PZT segments along the x direction can scavenge vibration energy at two harmonic frequencies. One may use different strategies to prevent cancelation such as altering polarization direction or segmented electrodes. But segmented PZT is the simplest way in terms of manufacturability. Each segment is connected by electrical wires to the energy collection circuit. This design platform is called a 'segment-type EH [30]'.

3.2. Design optimization

The design of a segment-type EH can be optimized to maximize an energy harvesting performance under a random bimodal excitation condition. Three other design challenges rather than the cancelation effect should be taken into account: (i) randomness in vibration ambient energy, (ii) structural durability and (iii) manufacturability. To overcome the challenges, this section introduces a robust optimization formulation in (4).

The initial design of the segment-type EH is constructed with two PZT segments (a total if four plates) and two proof masses as shown in figure 5. The optimization problem is formulated as follows:

$$\begin{aligned}
&\max P = \int_{\omega_I} P(\omega)\,\mathrm{d}\omega = \int_{\omega_I} P_g(\omega)\bar{A}^2(\omega)\,\mathrm{d}\omega \\
&= \int_{\omega_I} P_g(\omega)\left[\int_{\Omega_a} a^2(\omega) f_A(a(\omega))\,\mathrm{d}a\right]\mathrm{d}\omega, \qquad \text{or} \\
&V = \int_{\omega_I} V(\omega)\,\mathrm{d}\omega = \int_{\omega_I} V_g(\omega)\bar{A}(\omega)\,\mathrm{d}\omega \\
&= \int_{\omega_I} V_g(\omega)\left[\int_{\Omega_a} a(\omega) f_A(a(\omega))\,\mathrm{d}a\right]\mathrm{d}\omega \\
&s.t. \quad \sigma(FR_i) \leqslant \sigma_{\mathrm{DTS}} \\
&|FR_i - FR_i^0| \leqslant \delta
\end{aligned} \tag{4}$$

where ω_I is the frequency domain of interest, $P_g(\omega)$ and $V_g(\omega)$ are the power and voltage spectrum from harmonic analysis under a unit exciting acceleration $(1g)$, $\bar{A}(\omega)$ is the spectrum of the expected excitation amplitude (in g) in the frequency domain, $a(\omega)$ is the random variable of the excitation amplitude at a certain frequency ω, FR_i ith is the natural frequency of the harvester (with their target values FR_i^0), σ and σ_{DTS}, the maximum dynamic tensile stress and strength. This formulation maximizes the average power or voltage under random ambient vibration. This paper employs a linear piezoelectricity in which mechanical strain and resultant voltage is linearly proportional to the expected exciting acceleration, $\bar{A}(\omega)$. So the actual voltage spectrum is given by $V(\omega) = V_g(\omega)\bar{A}(\omega)$, while the power spectrum is given by $P(\omega) = P_g(\omega)\bar{A}^2(\omega)$ because of the relationship $P = V^2/R$ where R is external load. The objective function is calculated by integrating $P_g(\omega)\bar{A}^2(\omega)$ or $V_g(\omega)\bar{A}(\omega)$. The external load is set as 100 kΩ.

$a(\omega)$ has random nature and is differently configured from different ambient vibration sources such as HVAC systems,

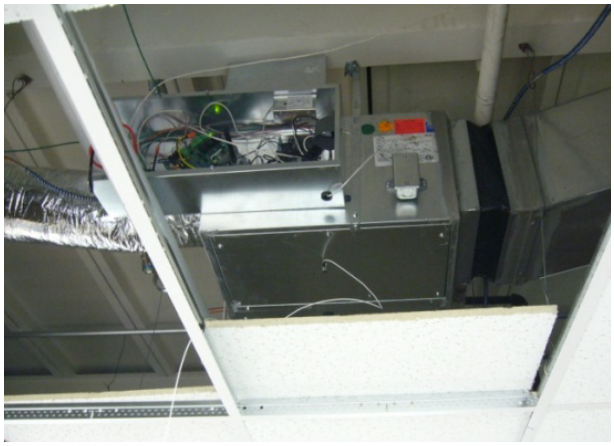

Figure 6. HVAC system.

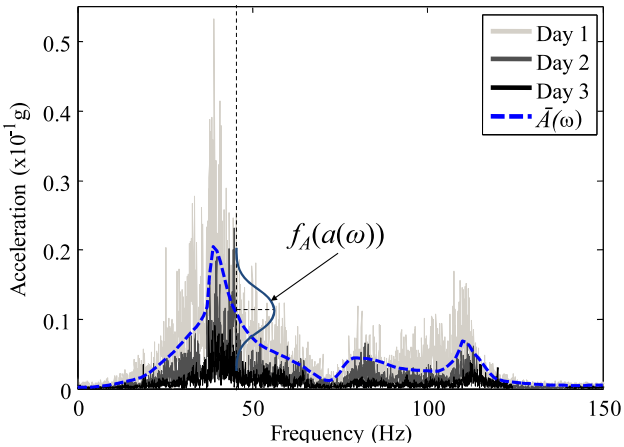

Figure 7. Measured excitation in frequency domain and its stochastic representation.

pipelines, bridges or, automobiles. In this paper the vibration from an HVAC system is chosen above the ceiling in an office (Engineering Lab building in the University of Maryland) as shown in figure 6. Time domain vibration signals are measured on three consecutive days (five times a day) and they are transformed into the frequency domain data by a fast Fourier transformation (FFT) as shown in figure 7. The amplitude at a certain frequency varies with every measurement, so the amplitude is randomly distributed as shown in figure 7 (around 50 Hz). $f_A(a(\omega))$ indicates the probability distribution of the amplitude at a certain frequency (ω). The rigorous formulation to calculate the expected power at a frequency is as written in (4). But the distribution of $f_A(a)$ is assumed to be symmetric in this paper and $\bar{A}(\omega)$ to be the collection of the mean values of $f_A(a)$. Therefore the optimization formulation can be simplified as follows:

$$\begin{aligned} \max P &= \int_{\omega_1} P_g(\omega)\bar{A}^2(\omega)\,\mathrm{d}\omega, \qquad \text{or} \\ V &= \int_{\omega_1} V_g(\omega)\bar{A}(\omega)\,\mathrm{d}\omega \\ s.t. \quad & \sigma(FR_i) \leqslant \sigma_{\mathrm{DTS}} \\ & |FR_i - FR_i^0| \leqslant \delta \end{aligned} \tag{5}$$

$\bar{A}(\omega)$ is approximated by interpolating 20 sampling points which are averaged values from the measurement as shown in figure 7. In general, the EH design problem targets to maximize electric power. On the other hand, this problem can be formulated to maximize a voltage (an alternative way) when the EH is specially designed for self-powered wireless sensors (for example, the temperature sensor requires 5.3 and 2.7 V for polling and data transmitting [19]). The durability constraint is described by limiting the maximum bending stress (σ) lower than the dynamic tensile strength ($\sigma_{\mathrm{DTS}} = 28$ MPa [12, 31]) where the maximum bending stress typically occurs in the middle of the clamped end.

There must be many local optimum designs without the constraint on the frequencies (the last equation in (5)). Among many, we believe that the global optimum must be found by placing the resonant frequencies of the EH (FR_i) at the excitation frequencies (FR_i^0). Therefore, the second constraint in (5) is very important to guide the optimization to the global optimum. Moreover we experienced that finding the feasible solution of (5) was difficult or highly time consuming. Therefore, the optimization is divided into two steps for fast convergence: (i) finding a feasible solution which satisfies the second constraint of (5) by simply minimizing $\Sigma_i|FR_i - FR_i^0|$ and (ii) solving the optimization problem in (5) starting from the feasible solution found in step (i) without the constraint on resonant frequency. The sequential quadratic program as an optimization algorithm in MATLAB software is used in this study.

Table 3. Design variables and bounds.

Design variable	Lower bound	Initial value	After frequency tuning	Optimal value	Upper bound
DV1	10.0 (mm)	18.5	21.4	**25.4**	25.4
DV2	10.0	18.5	21.2	**25.4**	25.4
DV3	5.0	16.2	5.0	5.0	25.4
DV4	2.0	14.7	23.1	**25.0**	25.0
DV5	2.0	9.2	3.8	5.0	15.0
DV6	10.0	32.0	21.7	16.1	50.0
DV7	10.0	59.5	61.0	57.0	100.0
DV8	6.0	11.0	11.5	**15.0**	15.0
DV9	5.7	8.1	7.5	7.8	10.0

Considering the manufacturability, the design platform of the segment-type EH is parameterized with nine design variables (DVs), as shown in figure 5: three widths (DV1 to DV3 at clamping end, intermediate mass and free end, respectively), height of each mass (DV4, DV5), length of each PZT segment (DV6, DV7) and length of each mass (DV8, DV9). Every edge of the PZT is set to form a straight line for easy manufacturing. Table 3 shows the design variables and their bounds. The upper bounds for the widths and mass heights are set to be 25.4 mm (1 inch) considering a compact housing design afterward.

The thickness of the PZT and brass center shim can be considered as design variables but they are fixed in this study

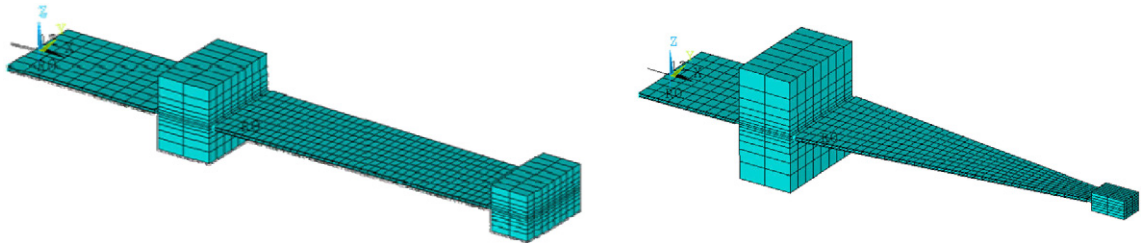

Figure 8. Initial and optimal design.

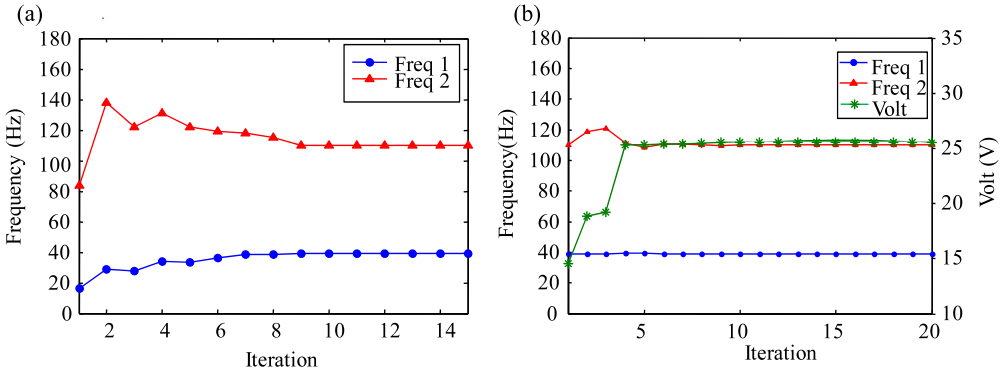

Figure 9. The optimization history. (a) First step to tune frequencies, (b) voltage maximization.

because we use a commercial PZT plate. The commercial PZT plate used in this study has 0.19 and 0.381 mm for PZT and brass center shim, respectively. The stainless steel is chosen for masses because of its relatively high density (7888 kg m^{-3}) and low cost. Additionally we need to track the first several mode shapes to configure FR_1 and FR_2 correctly throughout the design optimization process, because the order of the mode shapes may change due to a significant design change in the optimization. In the initial model, the first two vibration modes are bending modes, as shown in figure 4, and the third mode is the twisting mode (rotating with respect to the x axis in figure 4). During the optimization, the twist mode may become the second mode and the second bending mode as the third mode. Therefore we investigated the first several mode shapes for every iteration so that FR_1 and FR_2 match correctly to the resonant frequency of the first two bending modes.

3.3. Design optimization results and analysis

Figure 8 displays both initial (left) and optimal (right) designs, and the design variable change is summarized in table 3. In the final design, the length of the first mass (DV6) and the second PZT segment (DV5) becomes longer, while the second mass (DV7) and the first PZT segment (DV4) get shorter. Through this design change the inflection point is located at the first mass, which eliminates the cancelation. Because the maximum bending strain occurs at the first segment, it is beneficial to make the first segment wider and the first mass bigger. That is why DV1, DV2 and DV4 reach the upper bounds after the second optimization step (as indicated by bold fonts in table 3). For frequency tuning, the second segment becomes slender on approaching the free tip.

The optimization histories are plotted in figure 9. Figure 9(a) shows the history of the first two natural frequencies in the first optimization step. The frequencies are tuned from 16.2, 84.0 Hz to 39, 110 Hz after 15 iterations. The average voltage was increased from 14.2 to 25.2 V (the power was correspondingly improved from 25.5 to 65.3 μW) after 20 iteration, as shown in figure 9(b). The first and second mode shapes for the optimal design are shown in figure 10. The deforming configuration of the first mode is simply bending and no cancelation occurred. In the second mode the first mass is located at the inflection point and all PZT segments experience a pure bending so that no cancelation occurred.

The power spectra in the frequency domain ($P_g(\omega)$) are compared in figure 11. The spectra for the initial, the design after frequency tuning and the optimal model are plotted together with the exciting acceleration as a reference (the dashed line in figure 11, the same as $\bar{A}(\omega)$ from figure 7). The initial design (the thin dotted line) is changed into the design of which resonant frequency is tuned at FR_i^0 (the thick dotted line) and the optimal design afterward (the solid line). Figure 11 shows that the peak locations of the optimal design exactly agree with FR_i^0 (39, 110 Hz). The final optimum design shows the large amplitudes of power centered at both FR_1^0 and FR_2^0. Based on $P_g(\omega)$ in figure 11, the power generation from the second mode is 35.1%. It is apparent that the segment-type EH is quite effective in terms of energy harvesting. The maximum dynamic tensile stress at the center of the root is 1.18 MPa ($\sigma(FR_1)$) and 233 kPa ($\sigma(FR_2)$) which satisfies the durability constraint in (5).

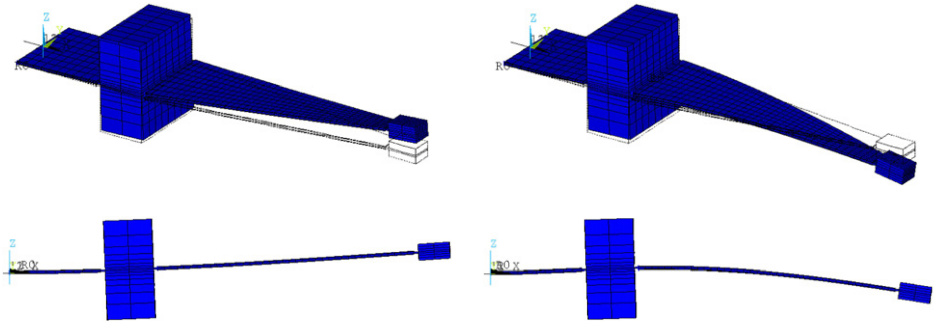

Figure 10. The first and second mode shapes of the segment-type EH.

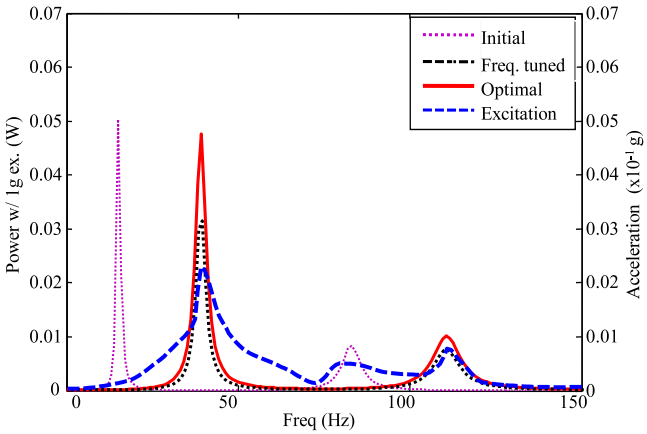

Figure 11. Power spectrum of initial and optimal EH.

4. Manufacturing

The optimized EH design in section 3 was manufactured for experimental evaluation of the performance. The manufacturing procedure is composed of three steps: machining, bonding and assembling.

4.1. Prototype machining process

For prototype manufacture, special care must be taken for dealing with PZT because it is very brittle. In particular, when we cut a PZT plate into a designated dimension it may crack very easily. To cut a PZT plate straight, it is scored by a precise utility knife very carefully first and a diamond blade is used to finish cutting afterward as shown in figure 12(a). One side of a PZT plate should be fully clamped, close to the cutting edge, to prevent unwanted cracking. A brass plate is ductile and less caution is required rather than for PZT, but the plastic deformation should be minimized during cutting and the cut edges should be polished evenly for easy assembly with PZT plates.

4.2. Plate bonding process

The electric potentials (or voltage) of the center shim and the electrodes facing the shim are all identical, so a conductive epoxy [32] is used to glue the machined PZT and the brass plate. Epoxy adhesive is applied to the brass plate in a thin layer by spreading with a knife blade. PZT plates are put on the layer and cured at 65 °C, 10 min in a hot chamber. A large and flat steel block is used to evenly press the specimen in the hot chamber. This process is repeatedly done for all four PZT plates. The curing procedure is summarized in figure 12(b).

4.3. Assembly and wiring process

After curing the epoxy may be squeezed out and it should be cleared to prevent electric conduction between any two electrodes. Methanol is applied in a soft swab to clean it. Proof masses are glued using a super glue gel and electric wires are soldered. Very thin and soft electric wires are chosen in order to minimize interrupting the vibration behavior of the EH. Before soldering a small amount of liquid solder flux (2 mm in diameter) is applied on the electrode of each PZT plate for easy adhesion of the solder. The final prototype is shown in figure 12(c) where the wires and the masses are all assembled.

5. Performance benchmark

The manufactured prototype has been evaluated in terms of the average power charged in 100 μF. The prototype is fixed on the top of a shaker and an accelerometer is attached to monitor the vibration amplitude of the shaker. Each PZT segment is separately rectified [33] so that the energy is not lost and summed up into a storage element. Figure 13 shows the block diagram of an EH circuit connected to the EH.

The input vibration signals are used to evaluate the charging performance (amplitude/frequency): case (a) 0.2g@39 Hz, (b) 0.2g@39 Hz + 0.1g@110 Hz, and (c) 0.2g@39 Hz + 0.2g@110 Hz. The charging curve for each case is displayed in figure 14. The fully discharged capacitor is then charged and the average power is estimated by the accumulated energy (0.5 CV^2, $C = 100$ μF) divided by the time duration (10 s). Two additional cases with different second frequency (with the same amplitude) are tried to investigate whether the segment-type EH makes use of the second excitation frequency (110 Hz): (d) 0.2g@39 Hz + 0.2g@80 Hz and (e) 0.2g@39 Hz + 0.2g@140 Hz.

Table 4 shows the power estimation for each case. By comparing cases (a)–(c), we can confirm that the power generation is significantly increased as the amplitude at

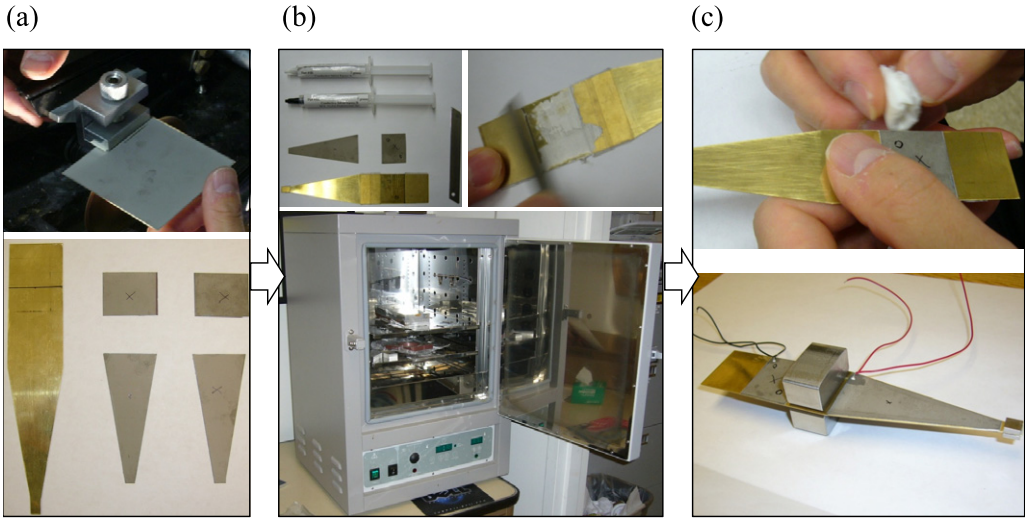

Figure 12. Manufacturing procedure of prototype. (a) Machining, (b) bonding, (c) finishing and assembly.

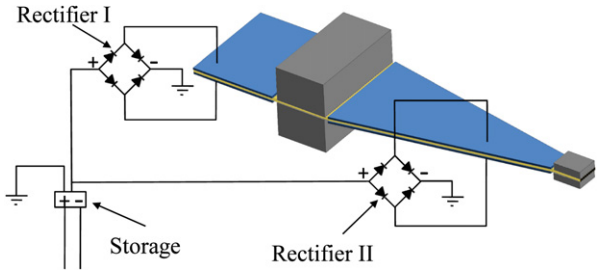

Figure 13. Block diagram of the EH circuit.

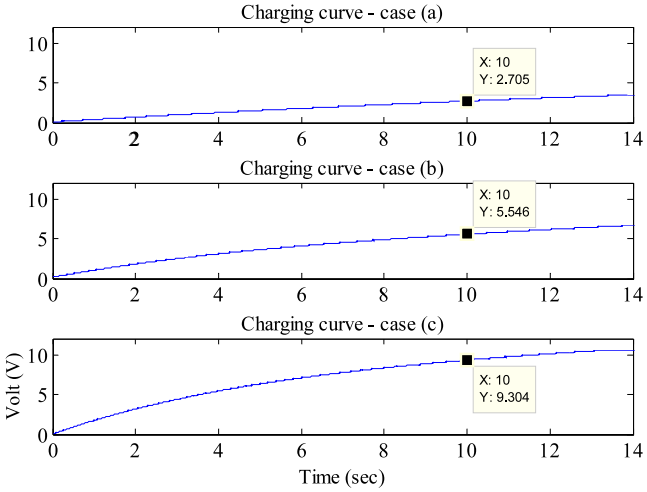

Figure 14. Charging curve for three different excitation conditions.

110 Hz increases, which shows the excellent performance of the segment-type harvester by showing its ability to utilize multiple resonant frequencies. The comparison through cases (c)–(e) shows that the EH effectively utilizes the second resonant frequency (110 Hz) rather than other frequencies (80, 140 Hz).

Figure 15 displays the open circuit voltage from each segment under 0.2g excitation. The first figure shows the voltage history at the first mode (39 Hz). The measured voltage amplitudes are 10.06 and 1.45 V from the first and the second segment, respectively. The phase angles of the two voltage signals are almost the same (the different is 15°). But in the second mode the phase difference between two voltage signals is 174° (the second figure in figure 15), which means they are canceled if not segmented. The amplitudes are 9.30 and 6.93V in this case.

Table 4. Power estimation of segment-type harvester.

Case (amplitude@frequency)	Power (μW)
(a) 0.2g@39 Hz	367
(b) 0.2g@39 Hz + 0.1g@110 Hz	1807
(c) 0.2g@39 Hz + 0.2g@110 Hz	3831
(d) 0.2g@39 Hz + 0.2g@ 80 Hz	758
(e) 0.2g@39 Hz + 0.2g@140 Hz	782

Table 4 and figure 15 show the excellent characteristics of the segment-type energy harvester. Some previous works on the energy harvesters for multimode utilization [34, 35] were simply the combination of multiple cantilevers, each of which was dedicated to a single frequency. So when one of the cantilevers becomes active to generate electrical energy at a certain frequency, the others stay idle. But the proposed design exploits the whole part of the piezoelectric material in any vibration mode under consideration which ensures more effective power generation.

6. Application to wireless sensor operation

The optimized segment-type EH is applied to produce electric energy from ambient vibration energy available in the HVAC system (see in figure 6). This electric energy can be used for supplying a power to operate wireless sensors for building automation (e.g., climate control). This study employs an analog temperature sensor node [19], which requires 5.3 V for initiating and 2.7 V for data transmitting. It requires about 15 μW for continuous temperature monitoring.

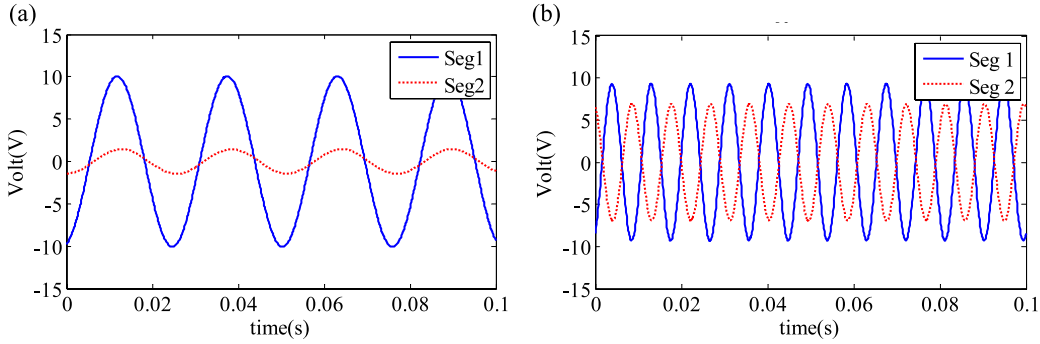

Figure 15. Open circuit voltages from each segment for both modes. (a) First mode, (b) second mode.

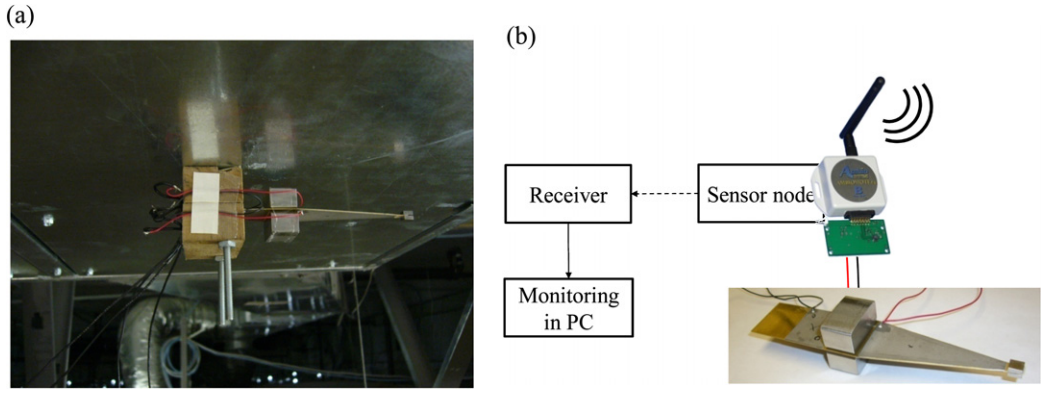

Figure 16. EH application to HVAC system. (a) EH attached at the bottom of HVAC housing, (b) connection of EH and wireless sensor,

6.1. Test set-up

The optimized segment-type EH is firmly clamped between two hardwood blocks that are attached at the bottom of the HVAC system (figure 16(a)). In addition to the connection of the electric components presented in figure 13, the sensor node is connected to the capacitor. Figure 16(b) shows a schematic view of the connection among the EH prototype, the EH circuit, the wireless sensor nodes (one with the analog temperature sensor and wireless sender, the other with the wireless receiver), and the monitoring system (USB connection from the receiver to a PC).

6.2. Effect of capacitance on EH charging performance

This study employed three different capacitance values (0.5, 2 and 100 μF) and the charging characteristics are compared as shown in figure 17. Data transmission rate is set to 1 Hz (1 transmission per second). The wireless transceiver waits for the capacitor voltage to charge up to 5.3 V ($=V_{\text{ini}}$) where the transmission initiates, and keeps transmitting while the voltage maintains more than 2.7 V ($=V_{\text{opr}}$). In general it takes longer to change up to a certain voltage as the capacitance increases and it is disadvantageous when frequent data transmission is required. For example, in the case of 100 μF it takes more than 700 s to charge from V_{opr} to V_{ini} and transmission is done in less than 50 s, on average. But by using a 0.5 μF capacitor a real-time temperature monitoring condition can be embodied; it takes only 8.8 s for charging and transmission is done for 2 s. The power estimation for each case is arranged in table 5. The least capacitance (0.5 μF) shows the most frequent transmission but the charging efficiency to a capacitor is the worst according to table 5. A reader can see the movie clip from a website on this temperature sensor operation powered by segment-type EH [36].

Table 5. Power estimation of EH from HVAC system vibration.

Capacitor (C) (μF)	Charge time (T)[a] (s)	Power (P)[b] (μW)
0.5	8.8	0.6
2	22.2	0.9
100	700	1.5

[a] Time to charge from V_{opr} to V_{ini}.
[b] 0.5C (V_{ini}^2–V_{opr}^2)/T.

6.3. Discussion on HVAC system application

Due to the random nature of HVAC system vibration, the vibration frequency provided to EH and the power generated by EH may vary randomly. Therefore it is not easy to decide the optimal external resistance in a deterministic manner. If we mainly consider the charging performance under a fixed vibration frequency, the optimal condition for the maximum power flow to the resistor can be found based on (6) [37–39] as

$$Z = \frac{1}{2\pi f C_{\text{p}}} \tag{6}$$

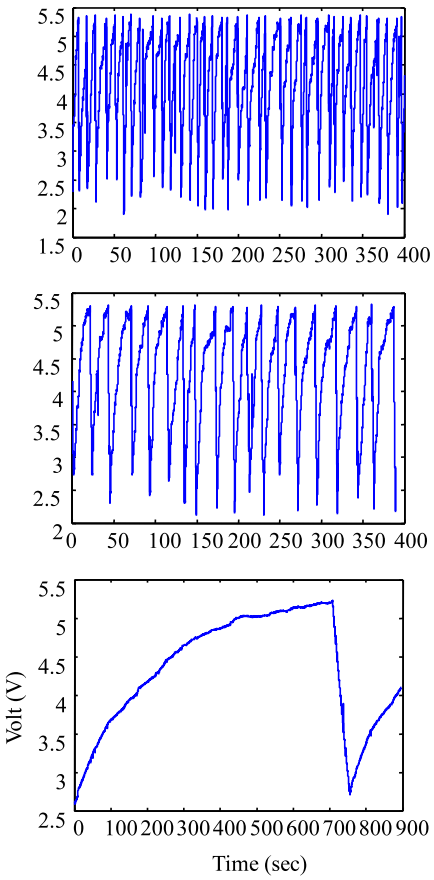

Figure 17. Charging/discharging curve for three different capacitances.

where Z is the impedance of the external load, C_p the piezoelectric material inherent capacitance and f the excitation frequencies. But the HVAC vibration contains multiple resonant peaks, so Z may not be found exactly at $1/2\pi f_1 C_p$ or $1/2\pi f_2 C_p$ (f_1 and f_2 are the first and second resonant frequency of the EH.). The optimal loads (Z) for each segment can be found by treating each segment as an independent energy source, considering C_p of both segments and multiple exciting frequencies (f_i). This topic needs more study. We will thus leave this study for our future research.

A timely control of the charging/transmitting sequence will enhance the operation of wireless sensors so that we can obtain sensory data only when required and EH can spend time mostly on charging a battery. For this purpose an additional switching circuit [40, 41] may be involved, but in this case the additional power consumption by the switching circuit should be considered [16].

7. Conclusion

The innovative energy harvester (EH) design platform called the segment-type EH is proposed in this paper for utilizing multiple resonant frequencies and successfully demonstrated with the HVAC system for wireless sensor operation. To prevent the cancelation effect, the PZT plates are separated near the inflection point of mechanical strain at which the proof mass was attached. The FE model of the EH was carefully calibrated, which enables us to explore different designs in the design optimization with high fidelity. In the design optimization formulation, the stochastic representation of the excitation is considered to achieve robust electrical energy scavenging from random vibrations with multiple resonant peaks. The optimal EH prototype was manufactured and successfully demonstrated with the HVAC system to operate the wireless sensor for real-time temperature monitoring. In this case study the EH design was determined to maximize the voltage, since the sensor node requires a relatively high voltage (5.3 and 2.7 V for polling and data transmitting, respectively).

The HVAC system we utilized showed two resonant peaks in the frequency domain of interest, so the proposed harvester is composed of two segments. But in case more than three resonant peaks are utilized a different conceptual design should be brought to have more segments: for example, when utilizing the first three modes, PZT should be segmented at three different inflection points (1 from the second, and 2 from the third vibration mode). Of course the number of the modes should be chosen considering whether introducing higher modes is beneficial or not in terms of power generation.

The ongoing future work can be divided into two parts: electric circuit design and EH shape design. From the electric circuit point of view, better performance is expected by optimizing an electric component circuit, such as matching impedance between the piezoelectric device and the external load as discussed in section 6.3. A rechargeable battery can be added for larger recharge ability. In the design perspective, the manufactured EH has a relatively large height because of the first proof mass. For a compact design we plan to use high density materials such as tungsten (about 2.5 times higher than stainless steel). The EH size can also be reduced by imposing reasonable size constraints in the design optimization formulation while maintaining the resonant frequencies of the EH at multiple excitation frequencies. Other ambient vibration sources in a building other than the HVAC system need to be found so that we can operate the EHs to supply power to a group of wireless sensors for building automation.

References

[1] ITP sensors and automation: Low-cost vibration power harvesting for wireless sensors. (cited 2008 Dec 4) Available from http://www1.eere.energy.gov/industry/sensors_automation/pdfs/kcf_vibrationpower.pdf

[2] Roundy S, Wright P K and Rabaey J M 2004 *Energy Scavenging for Wireless Sensor Networks: With Special Focus on Vibrations* (Berlin: Springer)

[3] Glynne-Jones P, Beeby S P and White N M 2001 Towards a piezoelectric vibration-powered microgenerator *IEE Sci. Meas. Technol.* **148** 68–72

[4] Sterken T, Baert K, Van Hoof C, Puers R, Borghs G, Fiorini P, Mcp I and Leuven B 2004 Comparative modelling for vibration scavengers *Proc. IEEE Sensors 2004*

[5] Silk M G 1984 *Ultrasonic Transducers for Nondestructive Testing* (Bristol: Adam Hilger)

[6] Leland E S, Lai E M and Wright P K 2004 A self-powered wireless sensor for indoor environmental monitoring *Proc. WNCG Conf. (Austin, TX)*

[7] Roundy S, Wright P K and Rabaey J 2003 A study of low level vibrations as a power source for wireless sensor nodes *Comput. Commun.* **26** 1131–44

[8] Sodano H A, Park G and Inman D J 2004 Estimation of electric charge output for piezoelectric energy harvesting *Strain* **40** 49–58

[9] Chen S N, Wang G J and Chien M C 2006 Analytical modeling of piezoelectric vibration-induced micro power generator *Mechatronics* **16** 379–87

[10] Elvin N, Elvin A and Choi D H 2003 A self-powered damage detection sensor *J. Strain Anal. Eng. Des.* **38** 115–24

[11] Goldschmidtboeing F and Woias P 2008 Characterization of different beam shapes for piezoelectric energy harvesting *J. Micromech. Microeng.* **18** 104013

[12] Roundy S, Leland E S, Baker J, Carleton E, Reilly E, Lai E, Otis B, Rabaey J M, Wright P K and Sundararajan V 2005 Improving power output for vibration-based energy scavengers *IEEE Pervasive Comput.* **4** 28–36

[13] Zheng B, Chang C and Gea H C 2007 Topology optimization for piezoelectric energy harvesting devices. *Proc. 7th WCSMO Conf. (Seoul, Republic of Korea)*

[14] Umeda M, Nakamura K and Ueha S 1997 Energy storage characteristics of a piezo-generator using impact induced vibration *Japan. J. Appl. Phys.* **36** 3146–51

[15] Sodano H A, Inman D J and Park G 2005 Generation and storage of electricity from power harvesting devices *J. Intell. Mater. Syst. Struct.* **16** 67

[16] Sodano H A, Inman D J and Park G 2005 Comparison of piezoelectric energy harvesting devices for recharging batteries *J. Intell. Mater. Syst. Struct.* **16** 799

[17] Sodano H A, Lloyd J and Inman D J 2006 An experimental comparison between several active composite actuators for power generation *Smart Mater. Struct.* **15** 1211–6

[18] Granstrom J, Feenstra J, Sodano H A and Farinholt K 2007 Energy harvesting from a backpack instrumented with piezoelectric shoulder straps *Smart Mater. Struct.* **16** 1810–20

[19] Analog temperature sensor. (cited 2008 24 Jul) Available from: http://www.ambiosystems.com/index.php/Sensors/Analog-temperature-sensor/Detailed-product-flyer.html

[20] Shenck N S and Paradiso J A 2001 Energy scavenging with shoe-mounted piezoelectrics *IEEE Micro* **21** 30–42

[21] Mateu L and Moll F 2005 Optimum piezoelectric bending beam structures for energy harvesting using shoe inserts *J. Intell. Mater. Syst. Struct.* **16** 835

[22] Anton S R and Sodano H A 2007 A review of power harvesting using piezoelectric materials (2003–2006) *Smart Mater. Struct.* **16** 1

[23] Sodano H A, Inman D J and Park G 2004 A review of power harvesting from vibration using piezoelectric materials *Shock Vib. Dig.* **36** 197

[24] Piezo systems product catalog. (cited 2008 11 February) Available from http://piezo.com/catalog7B.pdf

[25] NI PCI-6251. (cited 2008 11 March) Available from: http://sine.ni.com/nips/cds/view/p/lang/en/nid/14124

[26] James M L, Smith G M, Wolford J C and Whaley P W 1994 *Vibration of Mechanical and Structural Systems* (New York: Harper and Row)

[27] Lee S, Youn B D and Sodano H A 2008 Computer model calibration and design comparison on piezoelectric energy harvester *Proc. 12th AIAA/ISSMO Multidisciplinary Analysis and Optimization Conference (Victoria)*

[28] Properties of piezo material lead zirconate titanate (pzt-5a). (cited 2008 3 Mar) Available from: http://www.efunda.com/Materials/piezo/material_data/matdata_output.cfm?Material_ID=PZT-5A

[29] 2005 *ANSYS. 10.0* (Canonsburg, PA: ANSYS)

[30] Youn B D and Lee S 2008 *US Patent Specification* PS-2008-088 University of Maryland, Segment type energy harvester

[31] Channel industries 5500 lead zirconate titanate piezoelectric. (cited 2008 24 Nov) Available from: http://www.matweb.com/search/DataSheet.aspx?MatGUID=5d102619be9745df96d50b9cb0f19f14

[32] Conductive silver epoxy-14 gm kit-se(cited 2008 Oct 11) Available from: http://www.semicro.org/index.asp?PageAction=VIEWPROD&ProdID=3&HS=1

[33] Churchill D I and Arms S W inventor Slotted beam piezoelectric composite *US Patent Specification* 2007/0114890 A1 (May 24)

[34] Malkin M C and Davis C I Harness, Dickey & Pierce P.L.C., Multi-frequency piezoelectric energy harvester *US Patent Specification* 2004/0075363 A1 (Apr 22)

[35] Liu Y Honeywell International Inc., Energy harvesting device and methods *US Patent Specification* 2007/0125176 A1 (June 7)

[36] Intelligent System Reliability & Design Laboratory, University of Maryland. (cited 2009 May 11) Available from: http://terpconnect.umd.edu/~bdyoun/researches_EH_files/c_c_P1030812.mpg

[37] Ottman G K, Hofmann H F, Bhatt A C and Lesieutre G A 2002 Adaptive piezoelectric energy harvesting circuit for wireless remote power supply *IEEE Trans. Power Electron.* **17** 669–76

[38] Kim H, Priya S, Stephanou H and Uchino K 2007 Consideration of impedance matching techniques for efficient piezoelectric energy harvesting *IEEE Trans. Ultrason. Ferroelectr. Freq. Control* **54** 1851–9

[39] Lu F, Lee H P and Lim S P 2004 Modeling and analysis of micro piezoelectric power generators for micro-electromechanical-systems applications *Smart Mater. Struct.* **13** 57–63

[40] Ottman G K, Hofmann H F and Lesieutre G A 2003 Optimized piezoelectric energy harvesting circuit using step-down converter in discontinuous conduction mode *IEEE Trans. Power Electron.* **18** 696–703

[41] Guan M J and Liao W H 2007 On the efficiencies of piezoelectric energy harvesting circuits towards storage device voltages *Smart Mater. Struct.* **16** 498